PHYSICAL REVIEW APPLIED **18,** 044079 (2022)

Rotational Dynamics of a Looped-Tube Thermoacoustic Engine with a Flywheel

T. Watanabe,[1] E. Shoji,[1] T. Biwa,[1,*] and G. Penelet[2]

[1] *Department of Mechanical Systems Engineering, Tohoku University, Sendai 980-8579, Japan*
[2] *Laboratoire d'Acoustique de l'Université du Mans (LAUM), UMR 6613, Institut d'Acoustique–Graduate School (IA-GS), CNRS, Le Mans Université, Le Mans, France*

(Received 15 June 2022; revised 9 September 2022; accepted 15 September 2022; published 31 October 2022)

In a flywheel thermoacoustic engine, the rotating motion of the flywheel is sustained by the reciprocal motion of the working gas confined in an externally heated thermoacoustic engine. In this study, an equation of motion for the flywheel in the steady rotational state is derived and the key parameters governing the rotation dynamics of the looped-tube thermoacoustic engine loaded with a piston-flywheel assembly are investigated. We demonstrate that the relationship between the steady rotation frequency and the heating temperature is determined by the real part of the acoustic impedance of the engine subsystem. This result is in contrast to that of a conventional thermoacoustic engine with a linear load, where both the real and imaginary parts of the acoustic impedance impact the operating condition. When the flywheel is connected, the imaginary part of the acoustic impedance only affects the temporal fluctuation of the rotation frequency. The attainable shaft power that can be extracted from the engine is also discussed based on experimental results.

DOI: 10.1103/PhysRevApplied.18.044079

I. INTRODUCTION

Combined oscillations of the pressure and velocity of a gas column in a differentially heated flow channel can lead to the execution of a thermodynamic cycle, resulting in the generation of acoustic power from heat [1–3]. Classic examples include self-sustained oscillations in a Sondhauss tube [4,5] and in the He transfer tubes of a cryogenic system (known as Taconis oscillations [6,7]), where a steep temperature gradient along a gas-filled tube creates spontaneous acoustic oscillations of the gas column. Based on an understanding of this stability problem from a hydrodynamics perspective [8], recent studies have explored the concept of thermoacoustic Stirling engines [9–13] by using a regenerator and a pair of heat exchangers, both contained in a gas-filled looped-tube system. These engines simplify conventional mechanical Stirling engines because the traditional solid pistons are replaced with acoustic oscillations of the working gas.

The output acoustic power generated through the thermodynamic cycle can drive an acoustic load such as a linear alternator or an acoustic cooler [14–19]. These loads are connected to the looped-tube engine via a branch tube. The self-sustained oscillation occurs when a temperature difference between the ends of the regenerator exceeds a certain value. The oscillation amplitude increases with the temperature difference, whereas the oscillation frequency remains almost a constant value that is the natural frequency of the combined system consisting of the looped tube and the load. Therefore, as the input heat power to the engine is increased, the acoustic amplitude is increased, leading to the elevation of the output electrical power of a thermoacoustic electric generator and the cooling power of a heat-driven thermoacoustic cooler.

Previous studies have shown that the threshold temperature difference, the frequency, and even the growth in amplitude can be predicted from the temperature and frequency dependencies of the acoustic impedances of the subsystems at the connecting point [20–22]. The acoustic impedance is defined as the ratio of the complex amplitudes of the harmonic oscillations of the pressure and volume velocity of the gas in the branch tube between the looped tube and the linear load. We can then state that the operating condition of the thermoacoustic engine with a linear load is essentially reduced to the individual linear acoustic responses of the engine and load subsystems, although nonlinear phenomena such as minor loss [23–25] and chaotic oscillations [26,27] are encountered in the high-amplitude oscillation regime.

In a recent study, we have successfully demonstrated the operation of a thermoacoustic Stirling engine using a piston-crank-flywheel assembly [28] in which the looped-tube engine sustains the rotational motion of the flywheel. When a sufficiently high temperature difference

---

[*] tbiwa@tohoku.ac.jp

is created at the regenerator, the flywheel maintains its rotational motion after an external excitation is applied by hand. The rotational motion increases with the temperature difference, whereas the oscillation amplitude is mechanically fixed by the crank radius. We have numerically investigated the rotational motion of the combined system in a different study [29], where we have used the relation between the pressure and volume-velocity fluctuations in the time domain. This relation has been obtained from the frequency dependence of the acoustic impedance by applying a technique for system identification. The numerical results satisfactorily capture the complicated dynamics of the piston-flywheel assembly, which are essentially described by a nonlinear differential equation.

In this study, for a more intuitive understanding of a thermoacoustic engine driving a piston-crank-flywheel assembly, we simplify the equation of motion for the rotational motion of the piston-flywheel assembly to derive an energy-balance equation between the power supplied from the engine subsystem and the power loss of the load subsystem that consists of a piston and flywheel. We also use this equation to determine the relation between the rotational speed and the rotation angle, which provides a phase portrait of the rotation dynamics in the steady-rotation state. These relations are studied by the experiments individually designed for the looped-tube system and the piston-crank-flywheel assembly. The experimental results confirm the validity of our analysis on the rotational dynamics of the combined system. This study can help thermoacoustic scientists to design and build thermoacoustic engines capable of generating shaft power suitable for electricity conversion [30].

II. FLYWHEEL THERMOACOUSTIC ENGINE MODEL

Figure 1(a) shows a schematic of the flywheel thermoacoustic engine used in this study. It consists of two subsystems: one is the engine subsystem, which is a looped-tube thermoacoustic engine, and the other is the load subsystem, consisting of a piston-crank-flywheel assembly. These two subsystems are connected via a short branch tube.

To describe the reciprocal motion of the piston and the rotational motion of the flywheel, we use the rotation angle θ; θ is directed in a clockwise direction, as shown in Fig. 1(b), and $\theta = 0$ when the piston is at the bottom of the cylinder. The axial coordinate is directed upward, opposite to the gravitational acceleration g. The piston displacement x_p is given by

$$x_p = l - r\cos\theta, \tag{1}$$

where l is the length of the connecting rod and r is the crank radius ($l \gg r$).

The equation of motion for the rotational motion of the load subsystem is expressed as

$$(I + Mr^2\sin^2\theta)\ddot{\theta} + Mr^2\dot{\theta}^2\sin\theta\cos\theta + Mgr\sin\theta \\ = -rSp\sin\theta - rF_d\sin\theta\ \mathrm{sgn}(\dot{\theta}\sin\theta), \tag{2}$$

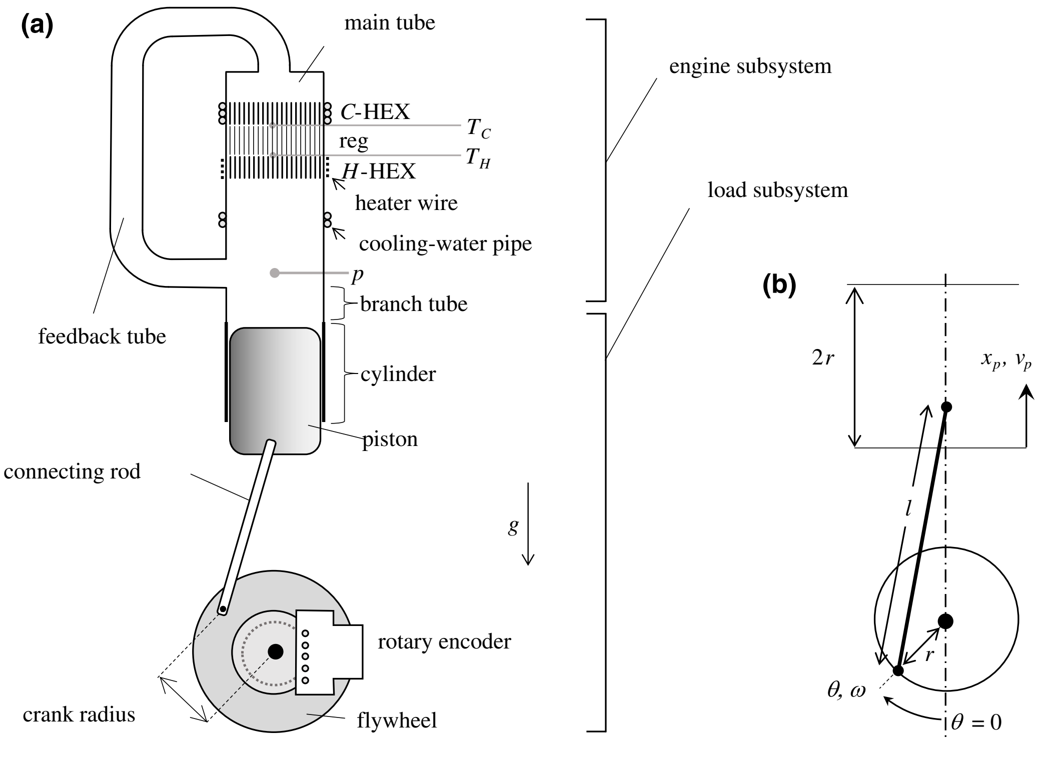

FIG. 1. (a) A schematic illustration of the flywheel thermoacoustic engine prototype. (b) The definition of the rotation angle θ, the angular frequency ω, and the displacement x.

where p is the excess pressure exerted on the piston and F_d is a constant that represents the friction losses in the piston-crank-flywheel assembly; M is the piston mass and S is the cross-section area of the cylinder. Equation (2) is essentially the same as Eq. (7) in our previous study [29]. For the current analysis, we simplify the equation of motion by replacing $\tanh(x)$ with the sign function $\mathrm{sgn}(x)$, where $\mathrm{sgn}(x) = 1$ when $x > 0$ and $\mathrm{sgn}(x) = -1$ when $x < 0$, whereas $\mathrm{sgn}(x) = 0$ when $x = 0$.

Consider the case when the combined system is in a steady rotational state. The angular velocity $\dot{\theta}$ can be expressed as $\dot{\theta} = \varpi + \omega'$, where ϖ denotes the temporal average and ω' represents the temporal fluctuation. For simplicity, ϖ is assumed positive throughout this study, although the negative value is also possible in the real system.

When ω' is sufficiently smaller than ϖ, we can state that

$$\theta = \varpi t,\ \dot{\theta} = \varpi,\ \ddot{\theta} = \dot{\omega}'. \tag{3}$$

In the piston-flywheel assembly configuration used in this study, we can safely ignore $Mr^2 \sin^2\theta$, because $Mr^2 \sin^2\theta \ll I$. Furthermore, when harmonic oscillations are assumed for the working gas in the looped-tube engine, we can consider the acoustic impedance to be $Z = P/V_p$, where P and V_p are the complex amplitudes of the acoustic pressure and volume velocity in front of the piston head, respectively. The positive V_p is directed to the loop. Because the piston velocity is $u_p = r\varpi \sin\varpi t = \mathrm{Re}[r\varpi \exp i(\varpi t - \pi/2)]$, the complex amplitude of the volume velocity ($= Su_p$) is expressed by $V_p = rS\varpi \exp(-i\pi/2)$. Therefore, the acoustic pressure $p = \mathrm{Re}[P \exp i(\varpi t)]$ is determined from the complex amplitude P

$$P = ZV_p = |Z| rS\varpi\ \exp[i(\Phi - \pi/2)], \tag{4}$$

where Φ represents the phase angle of Z.

These assumptions lead to the first-order ordinary differential equation for ω', which can be stated as

$$\begin{aligned} I\dot{\omega}' &+ \frac{Mr^2\varpi^2}{2}\sin 2\varpi t + Mgr\sin\varpi t \\ &= \frac{(rS)^2\varpi|Z|}{2}\left[\cos(2\varpi t + \Phi) - \cos\Phi\right] \\ &\quad - rF_d \sin\varpi t\ \mathrm{sgn}(\sin\varpi t). \end{aligned} \tag{5}$$

Equation (5) can be solved by integrating it over time. The solutions ϖ and ω' are (see the Appendix for the derivation)

$$-\frac{1}{2}(rS\varpi)^2\mathrm{Re}[Z] = 4rF_d\frac{\varpi}{2\pi} \tag{6}$$

and

$$\begin{aligned} \omega'(\theta) &= \frac{Mgr}{\varpi I}\cos\theta \\ &+ \left(\frac{Mr^2\varpi}{4I} + \frac{(rS)^2\mathrm{Im}[Z]}{4I}\right)\cos 2\theta \\ &+ \left(\frac{(rS)^2\mathrm{Re}[Z]}{4I} + 0.21\frac{F_d r}{\varpi I}\right)\sin 2\theta, \end{aligned} \tag{7}$$

where $\mathrm{Re}[Z]$ and $\mathrm{Im}[Z]$ denote $|Z|\cos\Phi$ and $|Z|\sin\Phi$, respectively.

Equation (6) represents the energy balance of the combined flywheel thermoacoustic system, where the left-hand side represents the acoustic power emitted from the loop W_{loop},

$$W_{\mathrm{loop}} = -\frac{1}{2}(rS\varpi)^2\mathrm{Re}[Z], \tag{8}$$

which travels from the engine subsystem to the load subsystem when $\mathrm{Re}[Z] < 0$. Here, $rS\varpi$ is the volume-velocity amplitude. The right-hand side represents the power loss W_{loss}, which is the power dissipation in the load subsystem and is defined as

$$W_{\mathrm{loss}} = 4rF_d\frac{\varpi}{2\pi}. \tag{9}$$

The physical meaning becomes clear by noting that the factor $4r$ denotes the total displacement of the reciprocal piston per cycle, F_d is the frictional force (assumed to be a constant), and $\varpi/(2\pi)$ is the number of rotations per unit time. The right-hand side of Eq. (9) thus depends on the friction model applied. If we adopt a more sophisticated friction model [31], the expression should be different. Indeed, the measured W_{loss} exhibits a different behavior from that of the simplified model defined by Eq. (2), as discussed in Sec. IV B.

Equation (7) describes the phase portrait of the rotating motion [32] on the ω-θ plane, where $\omega = \varpi + \omega'$. The temporal fluctuation ω' depends on both $\mathrm{Re}[Z]$ and $\mathrm{Im}[Z]$, although $\mathrm{Im}[Z]$ has no impact on the energy-balance equation given by Eq. (6) that determines ϖ. The objective of this study is to describe the combined flywheel thermoacoustic system using Eqs. (6) and (7). For this purpose, we determine W_{loop}, W_{loss}, and the unknown parameters Z and F_d in Sec. IV.

III. EXPERIMENTAL SETUP

The flywheel thermoacoustic engine in Fig. 1 is built for the experimental verification of our analysis. The engine subsystem consists of a main tube with an inner diameter of 40 mm and a feedback tube with an inner diameter of 12 mm. The length of the loop is 672 mm

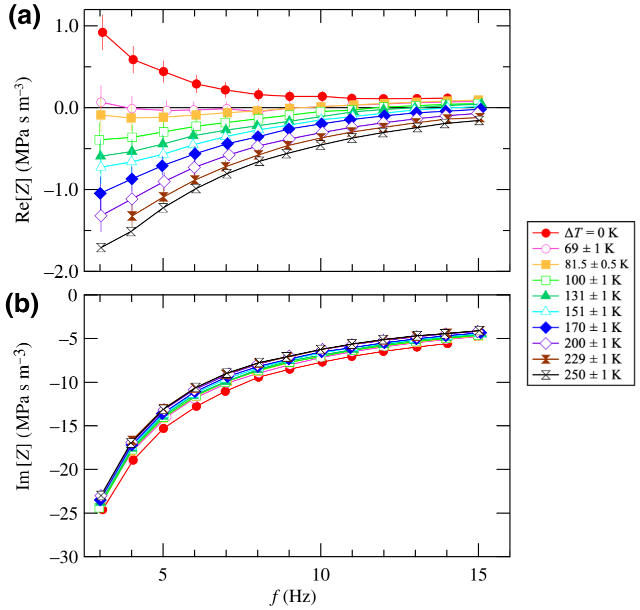

FIG. 2. The real and imaginary parts of the measured acoustic impedance as a function of the frequency f : (a) Re[Z]; (b) Im[Z]. The curves are drawn for a temperature difference ΔT over the range from 0 K to 250 K.

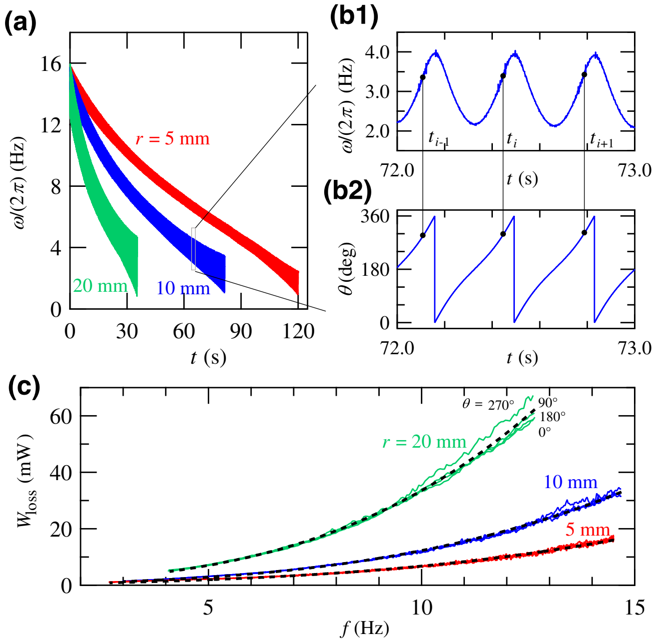

FIG. 3. (a) The temporal change of the rotation frequency observed in the freely rotating state of the piston-flywheel assembly. (b) Close-ups of the (b1) ω-t and (b2) θ-t relations for the 10-mm curve, respectively. (c) The power consumption derived from the temporal behavior as a function of the rotation frequency. The curve-fitting results are shown by dashed curves.

along the centerline. The regenerator is constructed using a 35-mm-long stack of 30-mesh screens (0.22 mm wire diameter). The heat exchangers consist of parallel plates that are 15 mm in length and 0.5 mm in thickness. The plates are evenly aligned (1-mm spacing). The hot heat exchanger, located below the regenerator, is wrapped in electrical heater wire, whereas the cold heat exchanger at the top of the regenerator is wrapped by a cooling-water pipe. The cooling-water pipe is also used below the hot heat exchanger to avoid excess heating of the main tube near the branch-tube connection point. The working gas is air at atmospheric pressure. The gas temperature is maintained at ambient temperature, except in the region near the hot heat exchanger. Temperatures T_H and T_C at the sides of the regenerator are measured by thermocouples inserted in the main tube.

The load subsystem consists of a glass piston, a connecting rod, and a flywheel. The piston weighs $M = 0.16$ kg and measures 36 mm in diameter. It moves smoothly in a glass cylinder having a cross-section area $S = 1.02 \times 10^{-3}$ m^2. The connecting rod links the piston to a crankpin fixed on the flywheel. The crank radius r, indicating the distance between the crankpin and the rotation axis of the flywheel, is adjustable (5 mm, 10 mm, or 20 mm). The displacement amplitude of the reciprocating piston is set equal to r. The flywheel is a cylindrical brass disk weighing 0.24 kg and its mass moment of inertia is $I = 1.39 \times 10^{-4}$ kg m^2.

For the measurement of the acoustic pressure, we use a pressure transducer (DD104, JTEKT) placed on the branch-tube wall. The rotation angle θ and angular velocity $\omega = \dot{\theta}$ are measured using a rotary encoder module (MG-30, Microtech Laboratory Inc.) having a circular disk with 360 slits, a pulse counter (CNT723, Cocoresearch Inc.), and a frequency-to-voltage converter (KAZ-Mighty, Cocoresearch Inc.). The analog output voltages of the pressure-transducer amplifier, the pulse counter, and the frequency-to-voltage converter are recorded using a multichannel analog-to-digital converter connected to a personal computer. The signal from the rotary encoder is also monitored. The maximum rotation frequency used in this study is 15 Hz, because the mechanical vibrations become excessive above this frequency.

IV. DERIVATION OF MODEL PARAMETERS

A. Acoustic impedance

To measure the acoustic impedance Z, the flywheel thermoacoustic engine is maintained in a thermal steady state by steady heat input via the hot heat exchanger and cooling water at the cold heat exchanger. The cold heat exchanger temperature T_C is maintained at 296 K during the experiment. The crank radius is set to $r = 10$ mm for this measurement. The flywheel shaft is connected to an external motor using a pulley-belt combination. The flywheel is driven by the motor at a constant angular frequency, leading to gas oscillations in the looped tube at the

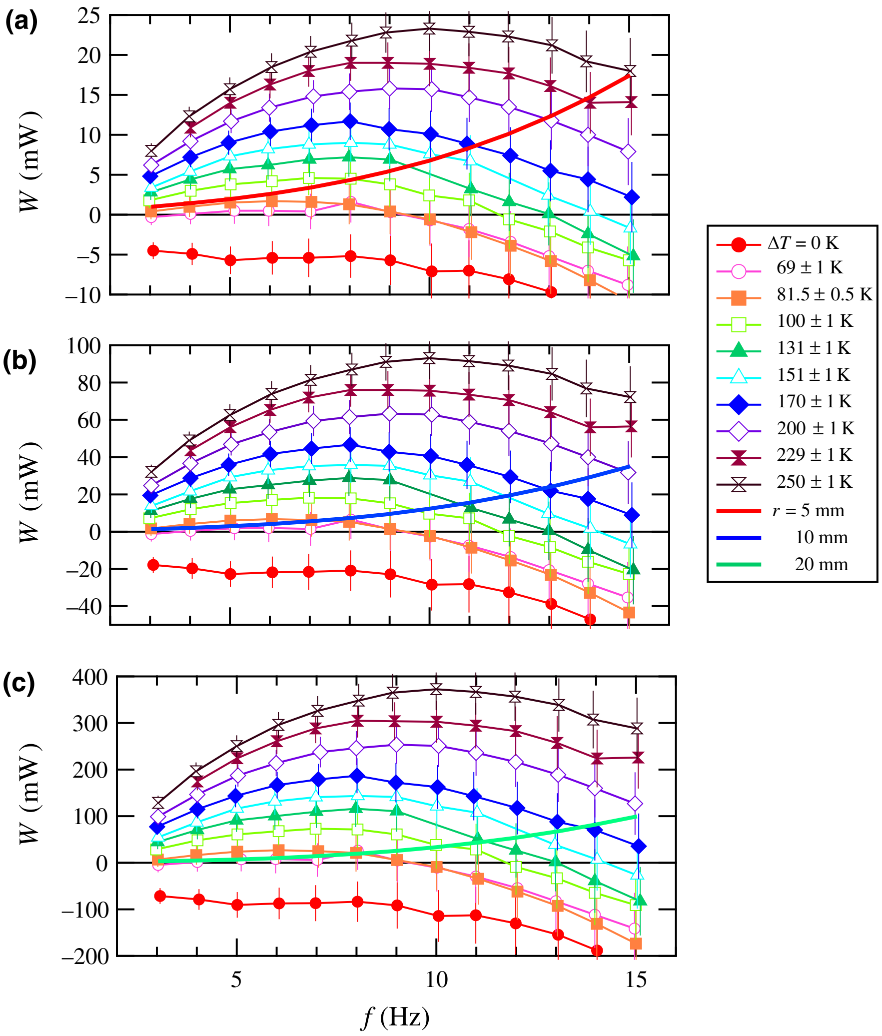

FIG. 4. The power supplied from the looped tube W_{loop} and the power consumption W_{loss} in the flywheel as a function of the rotation frequency when the crank radius is set to (a) 5 mm, (b) 10 mm, and (c) 20 mm. The power supply W_{loop} is determined for temperature differences ΔT from 0 K to 250 K; W_{loss} is the result of the curve fitting described in Sec. IV B.

same frequency. Temporal changes in crank angle $\theta(t)$ and acoustic pressure $p(t)$ are recorded. These measurements are repeated for various values of motor speed by elevating the temperature difference $\Delta T = T_H - T_C$ between the hot and cold heat exchanger temperatures from 0 K to 250 K.

The piston displacement $x_p(t)$ is derived by inserting the measured value of $\theta(t)$ into Eq. (1). From the sinusoidal curve fitting of $p(t)$ and $x_p(t)$, the oscillation frequency f, the respective amplitudes $|P|$ and $|X_p|$ of $p(t)$ and $x_p(t)$, and the phase lead of $p(t)$ relative to $x_p(t)$ $(= \Phi + \pi/2)$ are determined. The obtained displacement amplitude $|X_p|$ is very close to the nominal value ($r = 10$ mm), with a relative error of less than 1%. The amplitude $|V_p|$ of the volume velocity $v_p(t)$ is determined by $|V_p| = 2\pi f S|X_p|$. Finally, we obtain the acoustic impedance $Z = |P/V_p|\exp(i\Phi)$ for various sets of f and ΔT.

Figure 2 depicts the plots of (a) Re[Z] and (b) Im[Z] as functions of f parametrized using ΔT. The real part of Z, Re[Z], is consistently positive when $\Delta T = 0$ K because of energy dissipation due to thermoviscous losses in the looped tube. With increasing ΔT, Re[Z] becomes negative, meaning that the output power resulting from the thermoacoustic energy conversion in the regenerator region overcomes the energy dissipation in the looped tube. The imaginary part of Z, Im[Z], is consistently negative and inversely proportional to f, almost independent of ΔT, indicating that the looped tube can be regarded as an acoustic compliance rather than an acoustic inertance [33]. By using the derived acoustic impedance Z, we can estimate the acoustic power W_{loop} from Eq. (8) in addition to Re[Z] and Im[Z].

B. Loss parameters of the flywheel

Here, we consider the load subsystem alone, without any connection to the engine subsystem. The mechanical energy E of the load subsystem is given by the sum of the kinetic energies of the piston and flywheel and the potential energy due to gravity:

$$E = \frac{1}{2}M(r\omega\sin\theta)^2 + \frac{1}{2}I\omega^2 + Mg(l - r\cos\theta). \qquad (10)$$

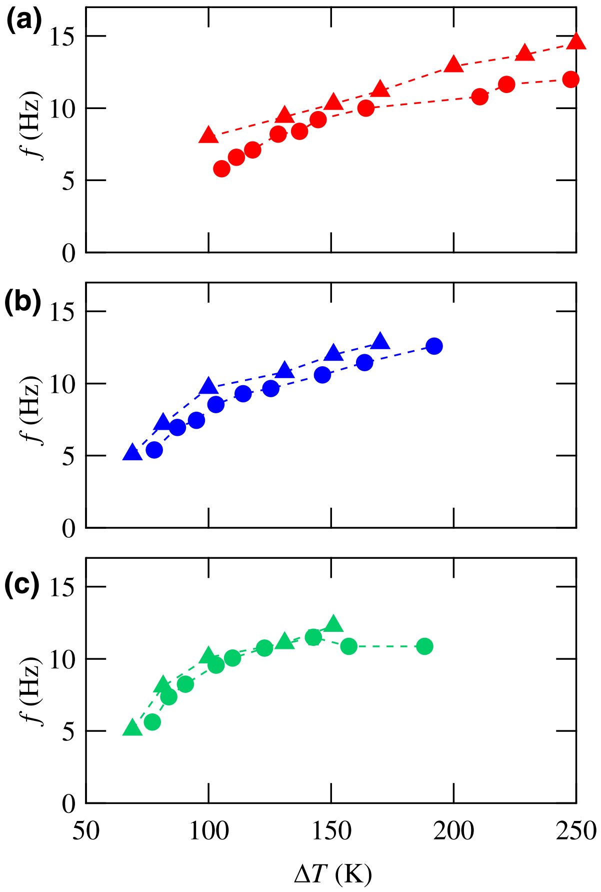

FIG. 5. The rotation frequency f as a function of the temperature difference ΔT: (a) $r = 5$ mm; (b) $r = 10$ mm; (c) $r = 20$ mm. The solid circles represent the frequencies observed in the combined flywheel thermoacoustic engine, whereas the triangles show the frequencies deduced from Fig. 4.

When the load subsystem is allowed to rotate freely after the initial manual rotation, E decreases with time, obeying

$$\frac{dE}{dt} = -W_{\text{loss}}. \tag{11}$$

Therefore, the measurement of ω and θ allows us to estimate the temporal change in E and then determine W_{loss} without relying on a specific friction model. It should be noted that Eq. (6) states the energy balance between the time-averaged power supply and loss. Hence, we determine W_{loss} using

$$W_{\text{loss}} = -\frac{E_{j+1} - E_{j-1}}{t_{j+1} - t_{j-1}}, \tag{12}$$

where t_j is the jth time when θ reaches a certain angle θ^* and E_j denotes the mechanical energy E when $t = t_j$.

Figure 3(a) shows the temporal changes in ω and θ for $r = 5$ mm, 10 mm, and 20 mm, observed experimentally in the load subsystem. Figures 3(b1) and 3(b2), respectively, represent the magnified views of the ω-t relation and the simultaneously determined θ-t relation for $r = 10$ mm. Additionally, the times t_j and $t_{j\pm1}$ when θ^* is set to 270° are shown. The values of ω at $t_{j\pm1}$ are adopted in the derivation of $E_{j\pm1}$ using Eq. (10).

The power loss W_{loss} is depicted as a function of the rotation frequency $f = \overline{\omega}/(2\pi)$ in Fig. 3(c) for $r = 5$ mm, 10 mm, and 20 mm. The angle θ^* is chosen from 0°, 90°, 180°, or 270°. The results indicate that the experimental derivation of W_{loss} is almost independent of the choice of θ^*, as the curves appear to generally follow the universal curve specific to the corresponding crank radius r. Although Eq. (9) indicates that W_{loss} is a linear function of f, the experimental W_{loss} increases nonlinearly with f. This result indicates that the proposed model oversimplifies the actual friction mechanism. We apply a curve fitting analysis on the results and find that the curve

$$W_{\text{loss}} = a_1 f + a_3 f^3 \tag{13}$$

yields satisfactory results with the fewest modifications [34]. The fitting results are shown by the dashed curves in Fig. 3(c). The parameter F_d is determined from the coefficient a_1 of the fitting results. The experimental W_{loss} and F_d values thus obtained can then be used to analyze the energy balance and the ω-θ relation.

V. RESULTS AND DISCUSSION

A. Energy balance

The energy balance between W_{loop}, the power supplied from the loop, and W_{loss}, the power consumed by the piston-flywheel assembly, is plotted against the rotation frequency f in Figs. 4(a)–4(c) for the cases with crank radius $r = 5$ mm, 10 mm, and 20 mm. It should be noted that W_{loop} and W_{loss} are determined individually using the experiments described in Secs. IV A and IV B. We find that W_{loop} gradually increases with the temperature difference ΔT and reaches a maximum at a certain f. We also observe that W_{loss} monotonically increases with f, as shown in Fig. 3. More importantly, these curves have crossing points where the energy balance $W_{\text{loop}} = W_{\text{loss}}$ is satisfied.

We now focus on a crossing point when $\Delta T = 170$ K and $r = 5$ mm as an example. The frequency $f_s = 11$ Hz at that point yields the steady-rotation frequency of the present flywheel thermoacoustic engine. If the rotation frequency is below f_s, the engine will speed up because $W_{\text{loop}} > W_{\text{loss}}$, meaning that the excess power supply increases the rotation frequency. However, if the frequency is above f_s, the engine slows down until $f = f_s$ is reached because $W_{\text{loop}} < W_{\text{loss}}$. The frequency f_s represents the *stable* rotation frequency of the flywheel thermoacoustic engine because the rotation frequency approaches f_s after some time. Figures 5(a)–5(c) summarize the relation

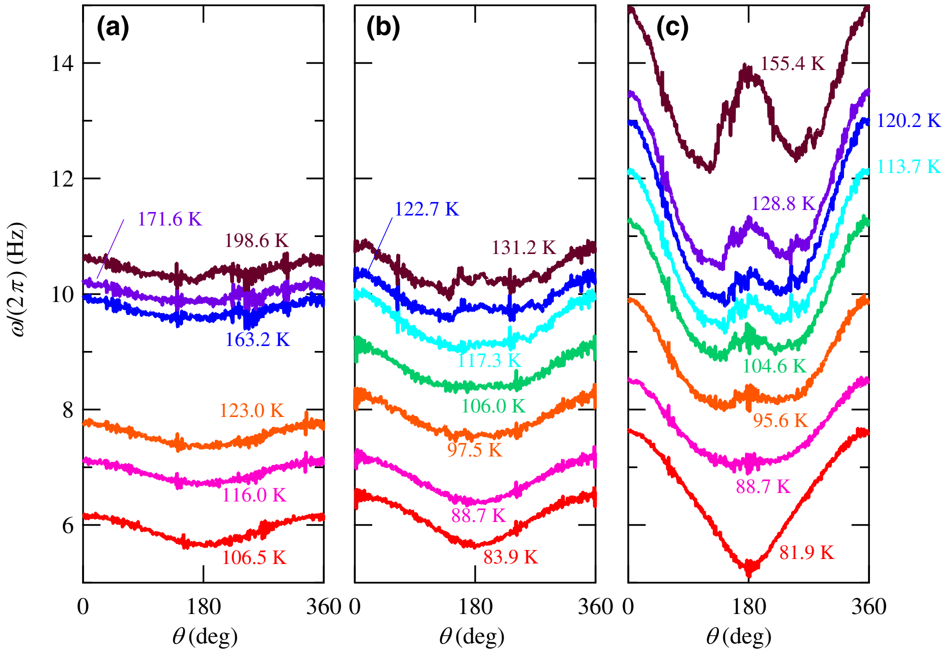

FIG. 6. The experimental ω-θ relation observed in the combined flywheel thermoacoustic engine when ΔT is changed: (a) $r = 5$ mm; (b) $r = 10$ mm; (c) $r = 20$ mm.

between f_s and ΔT and also illustrate the steady-rotation frequency versus ΔT that is experimentally obtained in the present flywheel thermoacoustic engine. We observe good agreement between f_s and the measured steady-rotation frequency, which provides experimental evidence that the rotation frequency of the flywheel thermoacoustic engine is determined through the energy-balance equation given by Eq. (6).

It is worth noting that a secondary crossing point can be found in Fig. 4(b) when $f_u = 3$ Hz and $\Delta T = 81.5$ K. If f is slightly greater than f_u, then f increases because $W_{\mathrm{loop}} > W_{\mathrm{loss}}$; if f is slightly less than f_u, f decreases because $W_{\mathrm{loop}} < W_{\mathrm{loss}}$. That is, f moves away from f_u in both cases and the engine eventually ends up spinning at a rotation frequency of f_s or reaches its rest state when $f = 0$. Therefore, this point identifies the *unstable* rotation frequency. Indeed, a corresponding temporal change is observed in the flywheel engine, as reported in our previous study [28].

The energy balance shown in Fig. 4 provides a hint of how to increase the shaft power that can be extracted from the present flywheel engine. The shaft power is given by $\Delta W = W_{\mathrm{loop}} - W_{\mathrm{loss}}$ when the external load is connected to the shaft of the flywheel. When $\Delta T = 250$ K, the maximum shaft power $\Delta W = 18$ mW is achievable for $r = 5$ mm at $f = 8.9$ Hz. For the cases involving $r = 10$ mm and 20 mm, the values of the maximum shaft power ΔW are 82 mW and 340 mW, respectively, at $f = 8.9$ Hz. Thus, the attainable shaft power can be estimated before performing real experiments with an external load. Therefore, the energy-balance plot serves as a guide for selecting the most suitable external load.

B. ω-θ relation

Figures 6(a)–6(c) present the θ dependence of the instantaneous angular velocity ω for $r = 5$ mm, 10 mm, and 20 mm, respectively. The measurements are made using the flywheel thermoacoustic engine shown in Fig. 1, operated in the steady-rotation mode. The temporal average of ω increases with ΔT as shown in Fig. 5. In addition, the fluctuation of the instantaneous angular frequency ω is greater for $r = 20$ mm compared to that for $r = 5$ mm. We also note that a local maximum appears at $\theta = \pi$ when $r = 20$ mm, whereas a minimum is found at $\theta = \pi$ when $r = 5$ mm. Such rotational dynamics are correctly described by Eq. (7).

For comparison, we reproduce the ω-θ relation shown in Fig. 7 by inserting the experimentally obtained parameters Z and F_d into Eq. (7). The offset value is deduced from the average of ω in Fig. 6. The ω-θ relations in Fig. 7 are very close to those shown in Fig. 6, meaning that the rotation dynamics are essentially governed by Eq. (7), which is derived from the equation of motion. Investigation of each term on the right-hand side of Eq. (7) indicates that the term proportional to $\cos\theta$ is dominant when ω is small and the term proportional to $\cos 2\theta$ becomes dominant when ω becomes large. The local maximum at $\theta = \pi$ when $r = 20$ mm reflects the enhancement of the term $Mr^2\overline{\omega}/(4I)\cos 2\theta$ by a factor of r^2.

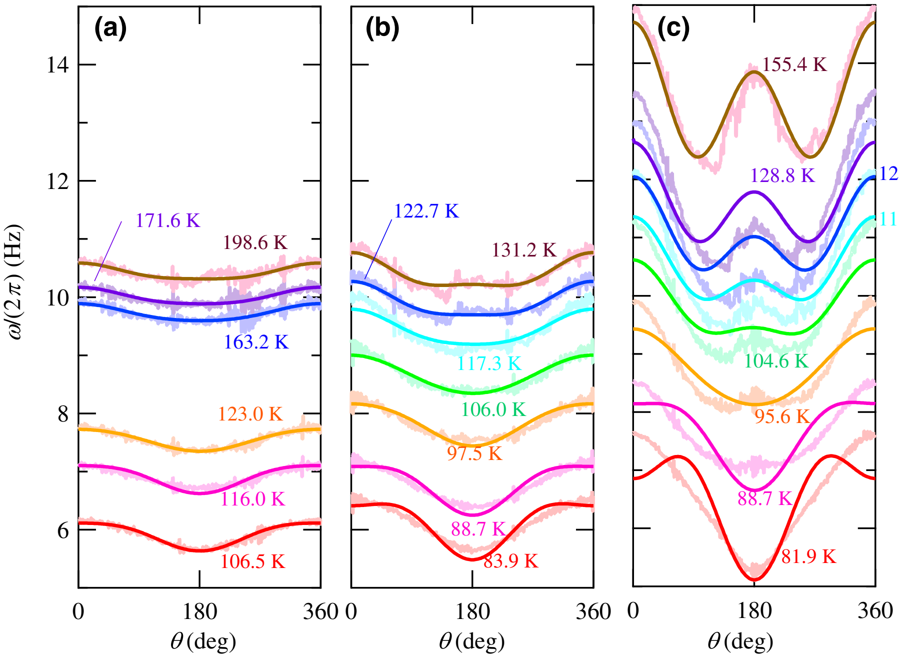

FIG. 7. The ω-θ relation estimated by using Eq. (7), for various ΔT values: (a) $r = 5$ mm; (b) $r = 10$ mm; (c) $r = 20$ mm. The experimental results observed in the flywheel thermoacoustic engine are replotted using pale colors for comparison.

We can now state that the rotation dynamics of the flywheel thermoacoustic engine are described well by Eqs. (6) and (7). In contrast, the working conditions of the thermoacoustic engine with a linear load are specified by the following relation:

$$Z_{\text{loop}} = Z_{\text{load}}, \tag{14}$$

where Z_{load} denotes the acoustic impedance of the linear load [20,21]. This relation originates from the continuity of the volume velocity and pressure at the connecting point of the looped tube and the linear load. Because the acoustic impedance is a complex quantity, Eq. (14) requires that $\text{Re}[Z_{\text{loop}}] = \text{Re}[Z_{\text{load}}]$ and $\text{Im}[Z_{\text{loop}}] = \text{Im}[Z_{\text{load}}]$. The first equation can be interpreted as the energy balance between the looped tube and the linear load. The second equation indicates that the working conditions are not determined solely by the energy balance. Therefore, one needs to adjust the inertance and compliance of the acoustic load. For a flywheel thermoacoustic engine, the energy balance is the necessary condition for the engine to operate. Therefore, an important quantity is $\text{Re}[Z]$ in the flywheel thermoacoustic engine. When $\text{Im}[Z]$ changes, ω' changes accordingly without changing the average rotation frequency $\overline{\omega}$. Therefore, one can concentrate on $\text{Re}[Z]$ when designing an engine subsystem using a looped tube. Such a difference may lead to a different looped-tube design based on whether it is connected to a linear or rotational load.

VI. CONCLUSIONS

To conclude, we derive the equation of motion for the flywheel under the assumption of a steady-rotation state and transform it into two equations: one for the energy balance and the other for the relation between the rotation speed and rotation angle. These equations are verified by the experimental results separately obtained for the engine and load subsystems. Specifically, the steady rotational frequency is determined by the real part of the acoustic impedance Z of the engine subsystem independent of the imaginary part of Z, whereas the imaginary part of Z only affects fluctuations in the rotational speed. The equation of motion given by Eq. (2) can also be used to discuss the libration motion [28] of a flywheel thermoacoustic engine. A more comprehensive study including a transition from libration motion to rotation motion is left for future research.

ACKNOWLEDGMENTS

This study was supported by the Japan Society for the Promotion of Science (JSPS) KAKENHI (Grant No. JP20H04383, 22K19861).

APPENDIX

We integrate Eq. (5) with respect to time, focusing on the sign reversal of $\text{sgn}(\sin\theta)$. The results are as follows:

$$\omega'(t) = A(t) - A(0) + B(t) + \omega'(0) \tag{A1}$$

for $0 \le t \le \pi/\varpi$ and

$$\omega'(t) = A(t) - A\left(\frac{\pi}{\varpi}\right) + C(t) + \omega'\left(\frac{\pi}{\varpi}\right) \tag{A2}$$

for $\pi/\varpi \le t \le 2\pi/\varpi$, where

$$A(t) = \frac{Mr^2\varpi}{4I}\cos 2\varpi t + \frac{Mgr}{\varpi I}\cos\varpi t + \frac{(rS)^2|Z|}{4I}\sin(2\varpi t + \Phi), \tag{A3}$$

$$B(t) = -\frac{(rS)^2\mathrm{Re}[Z]}{2I}\varpi t + \frac{F_d r}{\varpi I}(\cos\varpi t - 1), \tag{A4}$$

$$C(t) = -\frac{(rS)^2\mathrm{Re}[Z]}{2I}(\varpi t - \pi) + \frac{F_d r}{\varpi I}(-\cos\varpi t - 1). \tag{A5}$$

To obtain Eq. (6), we use the continuity of $\omega'(t)$. By letting $t = \pi/\varpi$ in Eq. (A1) and $t = 2\pi/\varpi$ in Eq. (A2), then

$$\omega'\left(\frac{\pi}{\varpi}\right) = A\left(\frac{\pi}{\varpi}\right) - A(0) + B\left(\frac{\pi}{\varpi}\right) + \omega'(0) \tag{A6}$$

and

$$\omega'\left(\frac{2\pi}{\varpi}\right) = A\left(\frac{2\pi}{\varpi}\right) - A\left(\frac{\pi}{\varpi}\right) + C\left(\frac{2\pi}{\varpi}\right) + \omega'\left(\frac{\pi}{\varpi}\right), \tag{A7}$$

respectively. Adding the equations and using $\omega'(0) = \omega'(2\pi/\varpi)$ and $A(2\pi/\varpi) = A(0)$ yields

$$B\left(\frac{\pi}{\varpi}\right) + C\left(\frac{2\pi}{\varpi}\right) = 0. \tag{A8}$$

Using Eqs. (A4) and (A5), we find that

$$\begin{aligned} B\left(\frac{\pi}{\varpi}\right) &= C\left(\frac{2\pi}{\varpi}\right) \\ &= -\frac{(rS)^2\mathrm{Re}[Z]}{2I}\pi - 2\frac{F_d r}{\varpi I} \\ &= 0, \end{aligned} \tag{A9}$$

from which we obtain Eq. (6).

To obtain Eq. (7), we use the relation

$$\int_0^{2\pi/\varpi} \omega'(t)\,dt = 0 \tag{A10}$$

and determine $\omega'(0)$ and $\omega'(\pi/\varpi)$. Inserting Eqs. (A1) and (A2) into the relationship above yields

$$\left[-A(0) + \omega'(0) - A\left(\frac{\pi}{\varpi}\right) + \omega'\left(\frac{\pi}{\varpi}\right)\right]\pi + \int_0^{\pi/\varpi} B(t)\,dt + \int_{\pi/\varpi}^{2\pi/\varpi} C(t)\,dt = 0. \tag{A11}$$

It is possible to show that

$$\int_0^{\pi/\varpi} B(t)\,dt + \int_{\pi/\varpi}^{2\pi/\varpi} C(t)\,dt = 0 \tag{A12}$$

after some calculations using Eqs. (A4) and (A5), and using Eq. (A9). Therefore, we are left with

$$\omega'\left(\frac{\pi}{\varpi}\right) = A(0) - \omega'(0) + A\left(\frac{\pi}{\varpi}\right). \tag{A13}$$

From a comparison with Eq. (A6), we can state that

$$\omega'(0) = A(0), \tag{A14}$$

such that

$$\omega'\left(\frac{\pi}{\varpi}\right) = A\left(\frac{\pi}{\varpi}\right). \tag{A15}$$

Finally, Eqs. (A1) and (A2) can be rewritten as

$$\omega'(t) = A(t) + \frac{F_d r}{\varpi I}\left(\cos\varpi t - 1 + \frac{2\varpi t}{\pi}\right) \tag{A16}$$

for $0 \le t \le \pi/\varpi$ and as

$$\omega'(t) = A(t) + \frac{F_d r}{\varpi I}\left[-\cos\varpi t - 1 + \frac{2(\varpi t - \pi)}{\pi}\right] \tag{A17}$$

for $\pi/\varpi \le t \le 2\pi/\varpi$.

Figure 8 presents the functions $G_1(t) = \cos\varpi t - 1 + 2\varpi t/\pi$ $(0 \le t \le \pi/\varpi)$ and $G_2(t) = -\cos\varpi t - 1 + [2(\varpi t - \pi)]/\pi$ $(\pi/\varpi \le t \le 2\pi/\varpi)$. It is found that two functions defined in different regions can be approximated by a single function of t. In this study, we use $D\sin 2\varpi t$, where $D = 0.21$ is determined by least-squares fitting. Therefore, the fluctuating part ω' can be expressed as

$$\omega'(t) = \frac{Mgr}{\varpi I}\cos\varpi t + \frac{Mr^2\varpi}{4I}\cos 2\varpi t + \frac{(rS)^2|Z|}{4I}\sin(2\varpi t + \Phi) + 0.21\frac{F_d r}{\varpi I}\sin 2\varpi t, \tag{A18}$$

which can be transformed into Eq. (7).

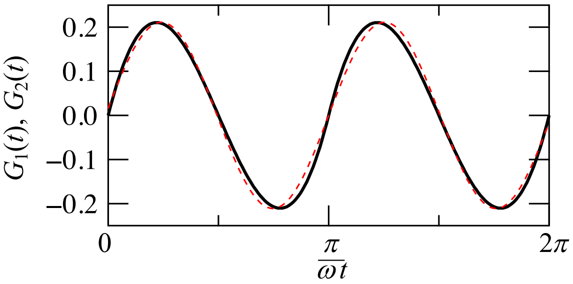

FIG. 8. The functions $G_1(t)$ and $G_2(t)$ (solid curves). The dashed curve shows the sine-fitting result.

[1] G. W. Swift, Thermoacoustic engines, J. Acoust. Soc. Am. **84**, 1145 (1988).

[2] A. Tominaga, Thermodynamic aspects of thermoacoustic theory, Cryogenics **35**, 427 (1995).

[3] T. Biwa, *Introduction to Thermoacoustic Devices* (World Scientific, Hackensack, NJ, USA, 2021).

[4] Lord Rayleigh, *The Theory of Sound* (Dover, New York, 1945).

[5] K. T. Feldman Jr., Review of the literature on Sondhauss thermoacoustic phenomena, J. Sound Vib. **7**, 71 (1968).

[6] K. W. Taconis, J. J. M. Beenakker, A. O. C. Nier, and L. T. Aldrich, Measurements concerning the vapour-liquid equilibrium of solutions of He^3 in He^4 below 2.19 K, Physica **15**, 733 (1949).

[7] T. Yazaki, A. Tominaga, and Y. Narahara, Experiments on thermally driven acoustic oscillations of gaseous helium, J. Low Temp. Phys. **41**, 45 (1980).

[8] N. Rott, Thermoacoustics, Adv. Appl. Mech. **20**, 135 (1980).

[9] T. Yazaki, A. Iwata, T. Maekawa, and A. Tominaga, Traveling Wave Thermoacoustic Engine in a Looped Tube, Phys. Rev. Lett. **81**, 3128 (1998).

[10] C. M. de Blok, Thermoacoustic system, Dutch Patent, International Application No. PCT/NL98/00515 (1998).

[11] S. Backhaus and G. W. Swift, A thermoacoustic Stirling heat engine, Nature **399**, 335 (1999).

[12] S. Backhaus and G. W. Swift, A thermoacoustic Stirling heat engine: A detailed study, J. Acoust. Soc. Am. **107**, 3148 (2000).

[13] H. Hyodo, S. Tamura, and T. Biwa, A looped-tube traveling-wave engine with liquid pistons, J. Appl. Phys. **122**, 114902 (2017).

[14] T. Yazaki, T. Biwa, and A. Tominaga, A pistonless Stirling cooler, Appl. Phys. Lett. **80**, 157 (2002).

[15] S. Backhaus, E. Tward, and M. Petach, Traveling-wave thermoacoustic electric generator, Appl. Phys. Lett. **85**, 1085 (2004).

[16] K. de Blok, Novel 4-Stage Traveling Wave Thermoacoustic Power Generator, ASME 2010 3rd Joint US-Eur. Fluid Eng. Summer Meet. Collocated With 8th Int. Conf. Nanochannels, Microchannels, and Minichannels, Am. Soc. Mech. Eng. **7**, 73 (2010).

[17] Z. Yu, A. J. Jaworski, and S. Backhaus, Travelling-wave thermoacoustic electricity generator using an ultra-compliant alternator for utilization of low-grade thermal energy, Appl. Energy **99**, 135-145 (2012).

[18] T. Bi, Z. Wu, L. Zhang, G. YU, E. Luo, and W. Dai, Development of a 5 kW traveling-wave thermoacoustic electric generator, Appl. Energy **185**, 1355-1361 (2017).

[19] M. Sharify and S. Hasegawa, Traveling-wave thermoacoustic refrigerator driven by a multistage traveling-wave thermoacoustic engine, Appl. Therm. Eng. **113**, 791-795 (2017).

[20] H. Hatori, T. Biwa, and T. Yazaki, How to build a loaded thermoacoustic engine, J. Appl. Phys. **111**, 074905 (2012).

[21] V. Zorgnotti, G. Penelet, G. Poignand, and S. L. Garrett, Prediction of limit cycle amplitudes in thermoacoustic engines by means of impedance measurements, J. Appl. Phys. **124**, 154901 (2018).

[22] Y. Kobayashi, S. Shinoda, T. Nakata, and N. Yamada, A unified stability analysis method for spontaneous oscillation conditions in thermoacoustic systems via measured frequency response data with application to standing- and traveling-wave engines, J. Sound Vib. **456**, 86-103 (2019).

[23] A. Petculescu and L. A. Wilen, Oscillatory flow in jet pumps: Nonlinear effects and minor losses, J. Acoust. Soc. Am. **113**, 1282 (2003).

[24] B. Smith and G. W. Swift, Power dissipation and time-averaged pressure in oscillating flow through a sudden area change, J. Acoust. Soc. Am. **113**, 2455 (2003).

[25] Y. Ueda, S. Yonemitsu, K. Ohashi, and T. Okamoto, Measurement and empirical evaluation of acoustic loss in tube with abrupt area change, J. Acoust. Soc. Am. **147**, 364 (2020).

[26] T. Yazaki, Experimental observation of thermoacoustic turbulence and universal properties at the quasiperiodic transition to chaos, Phys. Rev. E **48**, 1806 (1993).

[27] R. Delage, Y. Takayama, H. Hyodo, and T. Biwa, Observation of thermoacoustic chaotic oscillations in a looped tube, Chaos **29**, 093108 (2019).

[28] T. Biwa, T. Watanabe, and G. Penelet, Flywheel-based traveling-wave thermoacoustic engine, Appl. Phys. Lett. **117**, 243902 (2020).

[29] G. Penelet, T. Watanabe, and T. Biwa, Study of a thermoacoustic-Stirling engine connected to a piston-crank-flywheel assembly, J. Acoust. Soc. Am. **149**, 1674 (2021).

[30] M. A. G. Timmer, K. de Blok, and T. H. van der Meer, Review on the conversion of thermoacoustic power into electricity, J. Acoust. Soc. Am. **143**, 841 (2018).

[31] E. Pennestri, V. Rossi, P. Salvini, and P. P. Valentini, Review and comparison of dry friction force models, Nonlinear Dyn. **83**, 1785 (2016).

[32] S. H. Strogatz, *Nonlinear Dynamics and Chaos: With Applications to Physics, Biology, Chemistry, and Engineering* (Westview Press, Boulder, CO, 2001).

[33] G. W. Swift, *Thermoacoustics* (Springer International Publishing, New York, 2017).

[34] If we assume, additionally, a frictional torque $R\dot{\theta}$ on the right-hand side of Eq. (2), it results in the extra power loss of $R\bar{\omega}^2$. Although we try a curve fitting to $W = a_1 f + a_2 f^2$, the result is not satisfactory.